Wave equation migration velocity analysis for VTI models

Yunyue Li, Biondo Biondi, Robert Clapp and Dave Nichols

ABSTRACT

Anisotropic models are recognized as more realistic representations of the subsurface where a complex geological environment exists. These models are widely needed by all kinds of migration and interpretation schemes. In this paper, we extend the theory of wave equation migration velocity analysis (WEMVA) to build vertical transverse isotropic (VTI) models. Because of the ambiguity between depth and δ, we assume δ can be accurately obtained from other sources of information, and invert for the NMO slowness and the anellipticity parameter η. We use a differential semblance optimization objective function to evaluate the focusing of the prestack image in the subsurface-offset domain. To regularize the multi-parameter inversion, we build a framework to adapt the geological and the rock physics information to guide the updates in both NMO slowness and anisotropic parameter η. This regularization step is crucial to stabilize the inversion and to produce geologically meaningful results. We test the proposed approach on a 2-D Gulf of Mexico dataset starting with a fairly good initial anisotropic model. The inversion result reveals a shallow anomaly collocated in NMO velocity and η and improves both the continuity and the resolution of the final stacked image.

INTRODUCTION

When compared with isotropic models, anisotropic models are recognized as more realistic representations of the subsurface in complex geological environment (McCollum and Snell, 1932; Postma, 1955; Helbig, 1956). Many authors (Shan, 2009; Fletcher et al., 2009; Zhang and Zhang, 2009; Fei and Liner, 2008) have developed migration and processing schemes for vertical transverse isotropic (VTI) and tilted transverse isotropic (TTI) media; however, the challenge of building a reliable anisotropic Earth model remains the bottleneck for the exploration workflow.

Anisotropic model building tries to resolve more than one parameter at each grid point of the subsurface. This number could be 3 for VTI medium, and increase to 5 for TTI medium. Surface seismic data inversion becomes ill-posed and highly underdeterimined due to the rapidly increasing size of the model space with the increasing

Submitted for publication to Geophysics

complexity of the subsurface (Woodward et al., 2008; Bakulin et al., 2010b,a). To reduce the size of the model space, Sarkar and Tsvankin (2003, 2004) and Takanashi and Tsvankin (2012) parametrize their model space using factorized blocks or layers, where the anisotropic parameters ϵ and δ are constant and the velocity variations are simple linear or quadratic functions of the space coordinates. These factorization methods dramatically decrease the number of unknowns to be solved by the inversion, and hence stabilize the inversion. However, these models tend to over simplify the Earth where heterogeneities may occur at all scales.

In principle, grid-based tomographic methods handle both anisotropy and heterogeneity at the same time. Most of the existing grid-based anisotropic model-building schemes are based on ray-based tomography by measuring the non-hyperbolic moveout to flatten the common image gathers (CIG). The residual moveout is then back-projected along the ray paths to update the anisotropic models (Zhou et al., 2003, 2004; Yuan et al., 2006; Cai et al., 2009; Woodward et al., 2008). However, ray-based methods are prone to unrealistic results when multi-pathing exists in areas of complex overburden. Furthermore, due to the ill-posed and underdetermined nature of the anisotropic tomography, small amounts of noise in the residual moveout on a CIG gather can lead to significant variations in the inverted model. Therefore, we propose a wave-equation-based tomography method to build the anisotropic model.

In this paper, we first generalize the methodology of image-space WEMVA (Biondi and Sava, 1999; Sava and Biondi, 2004a,b) from an isotropic medium to an anisotropic medium. We use grid-based representations of NMO slowness, η and δ to parametrize the VTI medium, but keep δ fixed during the iterative WEMVA updates. We show that theoretically the gradient of the tomographic objective functional for an isotropic medium can be modified to describe an anisotropic medium by simply adding a term for additional parameters. To constrain the inversion, we precondition the model using geological and rock physics information. Finally, a field data test demonstrates that the proposed method can identify anomalies in the velocity and the anisotropic model, and hence produce a better migrated image with better spatial continuity and higher resolution.

WAVE EQUATION MIGRATION VELOCITY ANALYSIS FOR ANISOTROPY

In this section, we extend the methodology of WEMVA to the anisotropic medium. We provide a more concise derivation of the WEMVA gradients than a previous work (Li and Biondi, 2011) using the Lagrangian augmented functional instead of perturbation theory. The interpretations of the adjoint-state equations suggest the same implementation as perturbation theory suggests.

Governing equations

We parameterize the VTI subsurface using NMO slowness s_n, and Thomson parameter δ (Thomsen, 1986) and the anellipticity parameter η (Alkhalifah and Tsvankin, 1995). In the shot-profile domain, both source wavefields $\mathbf{D}$ and receiver wavefields $\mathbf{U}$ are downward continued using the following one-way wave equation and boundary condition (Shan, 2009):

$$\begin{cases} \left(\frac{1}{\sqrt{1+2\delta}}\frac{\partial}{\partial z} + i\Lambda\right) D(\mathbf{x},\mathbf{x}_s) = 0 \\ D(x,y,z=0,\mathbf{x}_s) = f_s\delta(\mathbf{x}-\mathbf{x}_s) \end{cases}, \tag{1}$$

and

$$\begin{cases} \left(\frac{1}{\sqrt{1+2\delta}}\frac{\partial}{\partial z} - i\Lambda\right) U(\mathbf{x},\mathbf{x}_s) = 0 \\ U(x,y,z=0,\mathbf{x}_s) = d_{\mathbf{x}_s}\delta(\mathbf{x}-\mathbf{x}_r) \end{cases}, \tag{2}$$

where f_s is the source wavelet, $d_{\mathbf{x}_s}$ is the shot record by a shot at $\mathbf{x} = \mathbf{x}_s$. We approximate the dispersion relation Λ of the VTI medium as follows:

$$\Lambda = \omega s_n \sqrt{1 - \frac{|\mathbf{k}|^2}{\omega^2 s_n^2 - 2\eta|\mathbf{k}|^2}}, \tag{3}$$

with $\mathbf{k} = k_x + k_y$. Equations 1 and 2 can be summarized in matrix forms as follows:

$$\mathbf{L}\mathbf{D} = \mathbf{f} \tag{4}$$

and

$$\mathbf{L}^*\mathbf{U} = \mathbf{d}, \tag{5}$$

where

$$\mathbf{f} = f_s\delta(\mathbf{x}-\mathbf{x}_s, z), \tag{6}$$

$$\mathbf{d} = d_{\mathbf{x}_s}\delta(\mathbf{x}-\mathbf{x}_r, z), \tag{7}$$

and

$$\mathbf{L} = \frac{1}{\sqrt{1+2\delta}}\frac{\partial}{\partial z} - i\Lambda. \tag{8}$$

It is well known that parameter δ is the least constrained by surface seismic data due to the lack of depth information. Therefore, we assume δ can be correctly obtained from other sources of information (such as check shots and well logs) and keep it fixed through the WEMVA iterations.

We use an extended imaging condition (Sava and Formel, 2006) to compute the image cube with subsurface offsets:

$$I_{\mathbf{h}} = (\mathbf{S}_{+\mathbf{h}}\mathbf{D})^*(\mathbf{S}_{-\mathbf{h}}\mathbf{U}), \tag{9}$$

where $\mathbf{S}_{+\mathbf{h}}$ is a shifting operator which shifts the wavefield $+\mathbf{h}$ in the $\mathbf{x}$ direction. Notice that $(\mathbf{S}_{+\mathbf{h}})^* = \mathbf{S}_{-\mathbf{h}}$. Equations 4, 5 and 9 are state equations, and $\mathbf{D}$, $\mathbf{U}$ and $I_{\mathbf{h}}$ are the state variables.

DSO gradients for anisotropic parameters

To evaluate the accuracy of the subsurface model, we use a DSO objective function (Symes and Carazzone, 1991; Shen, 2004):

$$J = \frac{1}{2}\sum_{\mathbf{h}} \langle \mathbf{h} I_{\mathbf{h}}, \mathbf{h} I_{\mathbf{h}} \rangle. \tag{10}$$

where $\mathbf{h}$ is the subsurface offset. In practice, other objective functions (linear transformations of the image) can be used rather than DSO. To derive the gradient of the DSO objective function with respect to s_n and η, we follow the recipe provided by Plessix (2006). First, we form the Lagrangian augmented functional:

$$\begin{aligned} \mathcal{L}(\mathbf{D}, \mathbf{U}, I_{\mathbf{h}}; \lambda, \mu, \gamma_{\mathbf{h}}; s_n, \eta) = & \qquad (11) \\ & \frac{1}{2}\sum_{\mathbf{h}} \langle \mathbf{h}\ I_{\mathbf{h}},\ \mathbf{h}\ I_{\mathbf{h}} \rangle \\ & + \langle \lambda,\ \mathbf{f} - \mathbf{L}(s_n, \eta)\mathbf{D} \rangle \\ & + \langle \mu,\ \mathbf{d} - \mathbf{L}^*(s_n, \eta)\mathbf{U} \rangle \\ & + \sum_{\mathbf{h}} \langle \gamma_{\mathbf{h}},\ (\mathbf{S}_{+\mathbf{h}}\mathbf{D})^*(\mathbf{S}_{-\mathbf{h}}\mathbf{U}) - I_{\mathbf{h}} \rangle\,. \qquad (12) \end{aligned}$$

Then the adjoint-state equations are obtained by taking the derivative of $\mathcal{L}$ with respect to state variables $\mathbf{D}$, $\mathbf{U}$ and $I_{\mathbf{h}}$:

$$\frac{\partial \mathcal{L}}{\partial \mathbf{D}} = -\mathbf{L}^*(s_n, \eta)\lambda + \sum_{\mathbf{h}} (\mathbf{S}_{+\mathbf{h}})^*(\mathbf{S}_{-\mathbf{h}}\mathbf{U})\gamma_{\mathbf{h}} = \mathbf{0}, \tag{13}$$

$$\frac{\partial \mathcal{L}}{\partial \mathbf{U}} = -\mathbf{L}(s_n, \eta)\mu + \sum_{\mathbf{h}} (\mathbf{S}_{-\mathbf{h}})^*(\mathbf{S}_{+\mathbf{h}}\mathbf{D})\gamma_{\mathbf{h}} = \mathbf{0}, \tag{14}$$

$$\frac{\partial \mathcal{L}}{\partial I_{\mathbf{h}}} = -\gamma_{\mathbf{h}} + \mathbf{h}^2 I_{\mathbf{h}} = 0, \forall\ \mathbf{h}. \tag{15}$$

Equation 13, 14, and 15 are the adjoint-state equations. Parameters λ, μ and $\gamma_{\mathbf{h}}$ are the adjoint-state variables, and can be calculated from the adjoint-state equations.

With the solutions to the equations above, we can now derive the gradients of the objective function 10 by taking the derivative of the augmented functional $\mathcal{L}$ with respect to the model variables s_n and η as follows:

$$\nabla_{s_n} J = \left\langle \lambda,\ -\frac{\partial \mathbf{L}}{\partial \mathbf{s_n}}\mathbf{D} \right\rangle + \left\langle \mu,\ -\frac{\partial \mathbf{L}^*}{\partial \mathbf{s_n}}\mathbf{U} \right\rangle \tag{16}$$

$$\nabla_{\eta} J = \left\langle \lambda,\ -\frac{\partial \mathbf{L}}{\partial \eta}\mathbf{D} \right\rangle + \left\langle \mu,\ -\frac{\partial \mathbf{L}^*}{\partial \eta}\mathbf{U} \right\rangle. \tag{17}$$

If the forward modeling operator $\mathbf{L}$ is isotropic, equation 16 reduces to the gradient of the isotropic DSO objective function with respect to the isotropic velocity. Therefore, the extension of WEMVA to the anisotropic medium is simply adding another term that is related to the additional anisotropic parameter.

Preconditioning the DSO gradient

Velocity model building is a highly underdetermined and nonlinear problem. Therefore, prior knowledge of the subsurface is needed to define a plausible subsurface model. Assuming Gaussian distribution, Tarantola (1984) characterizes the prior information using the mean and the covariance of the model and includes it as a regularization term. We separate the covariance into two parts, a spatial covariance between the same parameter at two different locations and a cross parameter covariance between different parameters at the same location. Physically, the spatial covariance describes the smoothness/roughness of the model parameter with respect to the space coordinates (Clapp, 2000; Woodward et al., 2008). In the multi-parameter anisotropic model estimation, spatial correlation lag for anisotropic parameters are considered longer than that for velocity (Woodward et al., 2008). Therefore, we can design different spatial smoothers for slowness and anisotropic parameters to reflect this prior information.

Moreover, given a certain lithology, velocity and anisotropic parameters are correlated with each other. Bachrach et al. (2011) shows that additional well log information also reduces the plausible range of correlations between the anisotropic parameters. Therefore, a local cross-parameter covariance is also necessary to include the prior lithological knowledge of the subsurface.

In this study, we assume the covariance of the model has two independent components: spatial covariance and local cross-parameter covariance (Li et al., 2011). In practice, instead of regularizing the inversion using Tarantola (1984), we use a preconditioning scheme (Claerbout, 2009) to speed up the convergence: smoothing filtering to approximate square-root of the spatial covariance, and a standard-deviation matrix to approximate the square-root of the cross-parameter covariance.

Mathematically, the preconditioning variable $\mathbf{n}$ is related to the original model $\mathbf{m}$ as follows:

$$\mathbf{m} = \mathbf{B}\mathbf{\Sigma}\mathbf{n}. \tag{18}$$

In equation 18, the smoothing operator $\mathbf{B}$ is a band-limited diagonal matrix:

$$\mathbf{B} = \begin{vmatrix} \mathbf{B}_s & 0 \\ 0 & \mathbf{B}_\eta \end{vmatrix}. \tag{19}$$

with different smoothing operators for NMO slowness and η, according to the geological information in the study area. The standard deviation matrix $\mathbf{\Sigma}$:

$$\mathbf{\Sigma} = \begin{vmatrix} \sigma_{\mathbf{ss}}\mathbf{I} & \sigma_{\mathbf{s}\eta}\mathbf{I} \\ \sigma_{\mathbf{s}\eta}\mathbf{I} & \sigma_{\eta\eta}\mathbf{I} \end{vmatrix}. \tag{20}$$

can be obtained by rock-physics modeling and/or lab measurements (Bachrach et al., 2011; Li et al., 2011). In an ideal case, we should estimate matrix $\mathbf{\Sigma}$ at each subsurface location to reflect the local lithological information.

The initial preconditioning model $\mathbf{n}_0$ is obtained by minimizing the following objective function:

$$J_{\text{init}} = \frac{1}{2} \langle \mathbf{m}_0 - \mathbf{B}\mathbf{\Sigma}\mathbf{n}_0, \mathbf{m}_0 - \mathbf{B}\mathbf{\Sigma}\mathbf{n}_0 \rangle . \tag{21}$$

The gradient of the objective function (10) with respect to this preconditioning variable $\mathbf{n}$ is

$$\begin{aligned} \nabla_{\mathbf{n}} J &= (\frac{\partial \mathbf{m}}{\partial \mathbf{n}})^* \nabla_{\mathbf{m}} J \\ &= \mathbf{\Sigma}^* \mathbf{B}^* \nabla_{\mathbf{m}} J, \end{aligned} \tag{22}$$

where $\nabla_{\mathbf{m}} J = [\nabla_{s_n} J \quad \nabla_{\eta} J]^T$. We use a nonlinear conjugate gradient algorithm to minimize the objective function.

FIELD DATA TESTS

Anisotropic parameters cannot be fully constrained by surface seismic data. Therefore, anisotropic models are better defined in well-developed and production areas, where various well log, check shots and VSP data are available. The Gulf of Mexico dataset used in this study is from a producing area in an offshore sedimentary basin close to a salt body. While vertical check shots and sonic logs best constrain the vertical velocity model, offset check shot (OCS) data, thanks to their long offset give information on both vertical and horizontal velocity. The current anisotropic model was built using an interactive visualization method (Bear et al., 2005) that integrates surface seismic, sonic logs, vertical check shots, and offset check shots.

We extract a 2-D line from the Gulf of Mexico dataset at a location where the salt body is far away. Source spacing is 100 m, and receiver spacing is 50 m. The maximum offset in this 2-D line is about 4 km. The initial stack image is shown on the top panel in Figure 4. Although the apparent dip is high due to the large vertical stretch (3 km in depth vs. 16 km on the horizontal axis), the reflectors in this 2-D line are fairly flat. We then estimate the dip field from the initial image and use it to precondition the gradient for both slowness and η. Due to the lack of rock physics information, a stationary matrix $\mathbf{\Sigma}$ with $\sigma_{\mathbf{s}\eta} = 0$ is applied in the preconditioning to scale the relative amplitude of the slowness and η gradient.

We can see many small-scale faults in this area on the top panel in Figure 4. Migration artifacts at $x = 13$ km and $z = 2500$ m are caused by a big vertical fault running from $x = 14$ km on the top to the bottom of the section. The initial angle gathers are shown in the bottom row in Figure 4. Since this is a streamer geometry, the subsurface reflectors are only illuminated from positive angles. Although the gathers are close to flat, we can still see upward residual moveouts in the angle domain. Therefore, we have a chance to improve the model and the image by flattening the gathers.

The inverted anisotropic model after 8 iterations is shown in figure 2. Updates between the initial and the inverted velocity and η models are shown in figure 3(a)

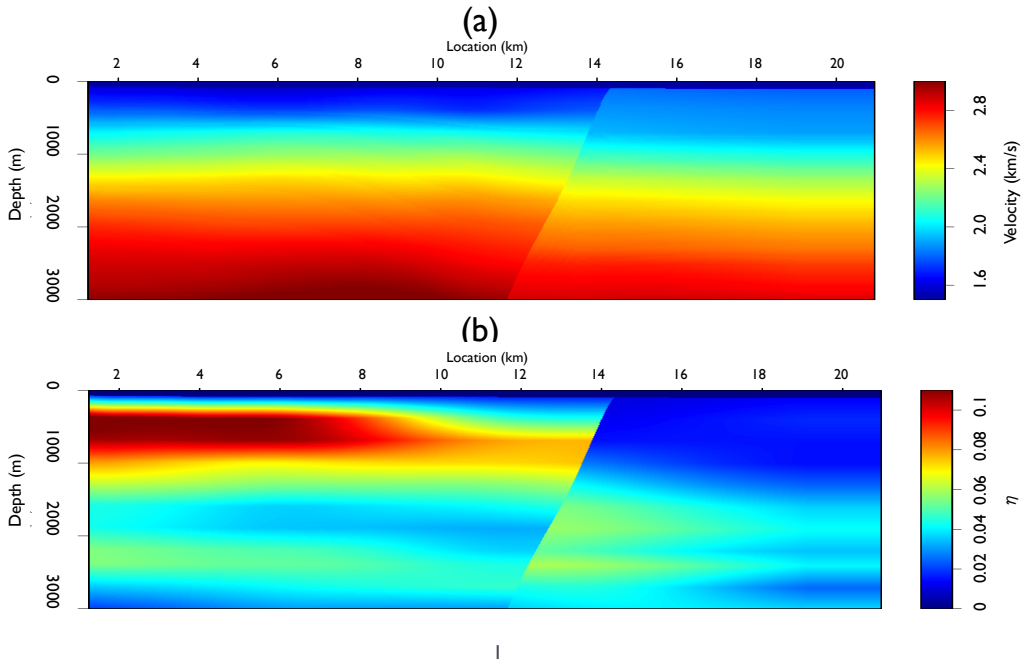

Figure 1: Initial velocity model (a) and initial η model (b). [**CR**]

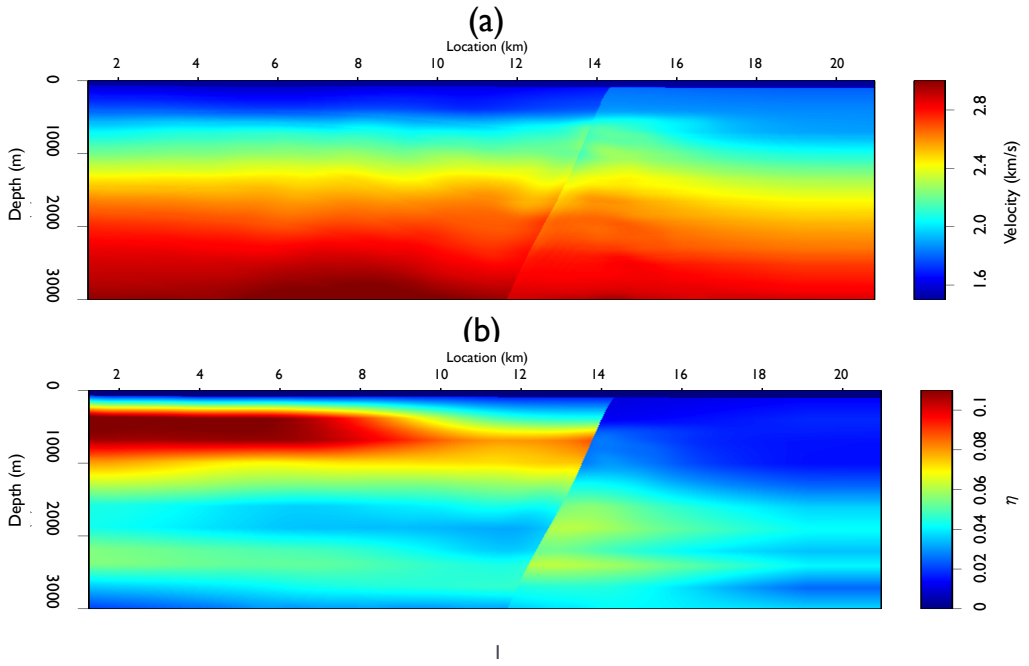

Figure 2: Inverted velocity model (a) and inverted η model (b). [**CR**]

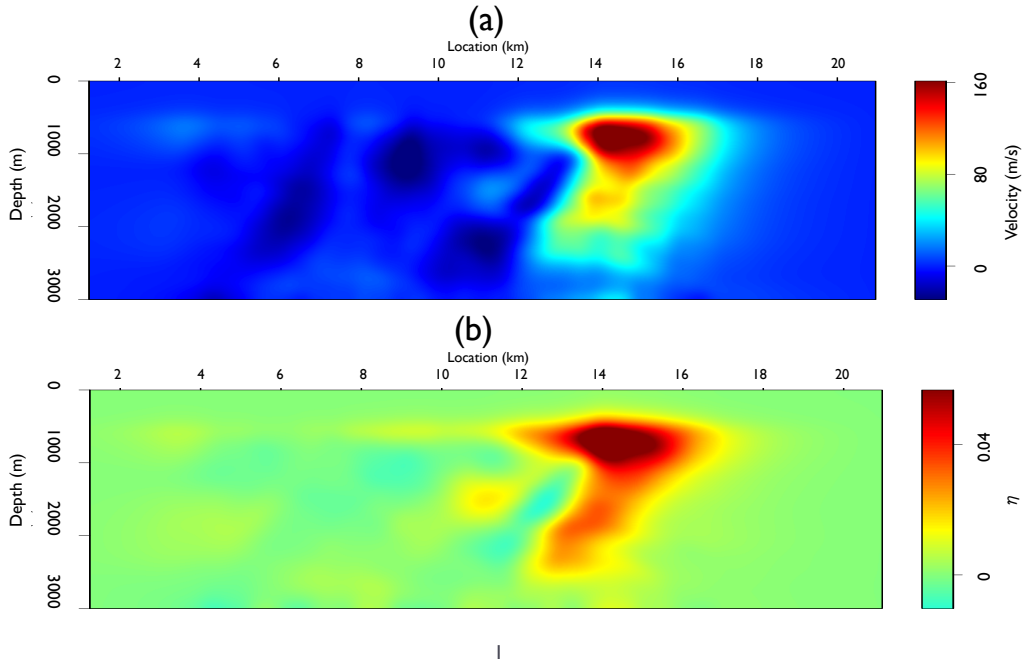

Figure 3: Updates in velocity model (a) and updates in η model (b) after inversion. [**CR**]

and 3(b), respectively. First, notice that we are able to resolve a localized shallow anomaly between 13 km and 15 km at around 800 m below surface. Also, notice that the updates in velocity are less than 10%, whereas the updates in η are around 25%. These positive updates in both velocity and η agree well with the negative travel time misfits in the previous OCS modeling results (Bear et al., 2005).

Comparing the initial stack image on the top panel in Figure 4 with the final stack image on the top panel of Figure 5, we can see improved continuity and signal strength in the area highlighted by the oval. The faulting in this area is also better defined in the final image. If we correlate the inverted models with the final migrated image, we may choose to change the interpretation of the major fault: the emerging location on the surface may be shifted from 14.2 km to around 16 km.

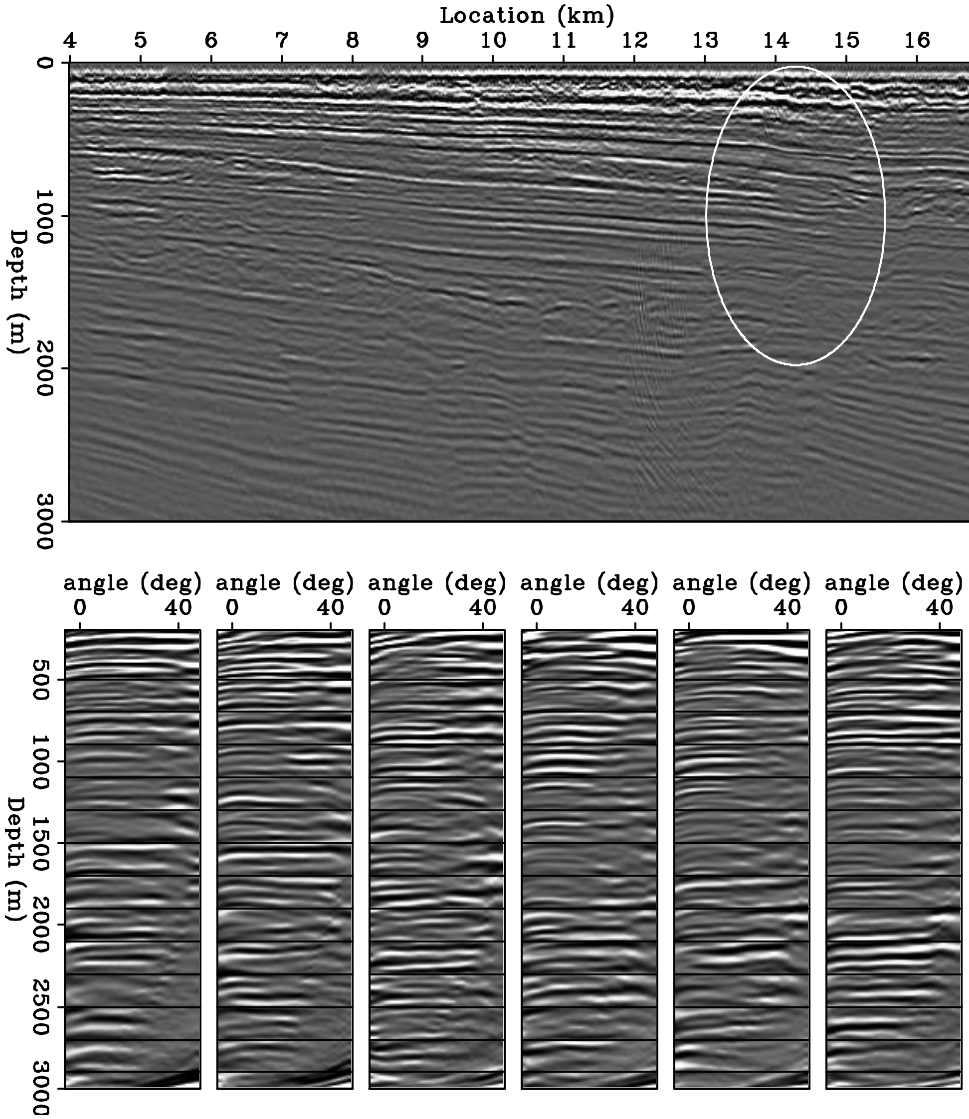

Figure 4: The initial stack image (Top panel) and initial angle domain common image gathers at CMP $= 7, 10, 13, 14, 14.5, 15$ km (Bottom row). [**CR**]

We can also verify the effect of the updates in velocity and η on the angle gathers at different CMP locations. The initial angle domain common image gathers (ADCIGs) are shown in the bottom row in Figure 4, and the final ADCIGs produced using the inverted models are shown in the bottom row in Figure 5. To better illustrate the effects of the model updates, the ADCIGs are sampled more densely between CMP = 13km and 16km and sparsely outside of this range. In general, we can see improved flatness for all the reflectors. Specifically, for the shallower events above 1km, most improvements happen at large angles over 35°. Therefore, we interpret the improvements for the shallow events primarily as the contribution of the improved η model.

For the deeper events at the same CMP location, both the depth and the flatness of the angle gather have been changed by inversion. The upward-curving events in the angle domain from the initial migration has been flattened by the improved velocity and η model.

CONCLUSIONS

We have presented a methodology of wave equation migration velocity analysis for anisotropic media. Our method is fully automated and picking-free. The grid-based parameterization for the velocity and anisotropic parameters provides the flexibility to reveal perturbations with different scales. The regularization scheme of our proposed method is crucial to obtain geological meaningful results for both velocity and anisotropic parameters. It is also the interface to include human interpretation and other prior knowledge. The test of our anisotropic WEMVA algorithm on a 2-D slice of a GoM field dataset produces improved stacked image with better continuity and higher resolution. Therefore, we believe our method provides a good model building tool for anisotropic media.

ACKNOWLEDGEMENT

The authors thank ExxonMobil for providing the field data and the sponsors of the Stanford Exploration Project for their financial support.

REFERENCES

Alkhalifah, T. and I. Tsvankin, 1995, Velocity analysis for transversely isotropic media: Geophysics, **60**, 1550–1566.

Bachrach, R., Y. K. Liu, M. Woodward, O. Zradrova, Y. Yang, and K. Osypov, 2011, Anisotropic velocity model building using rock physics: Comparison of compaction trends and check-shot-derived anisotropy in the gulf of mexico: SEG Expanded Abstract, **30**, 207–211.

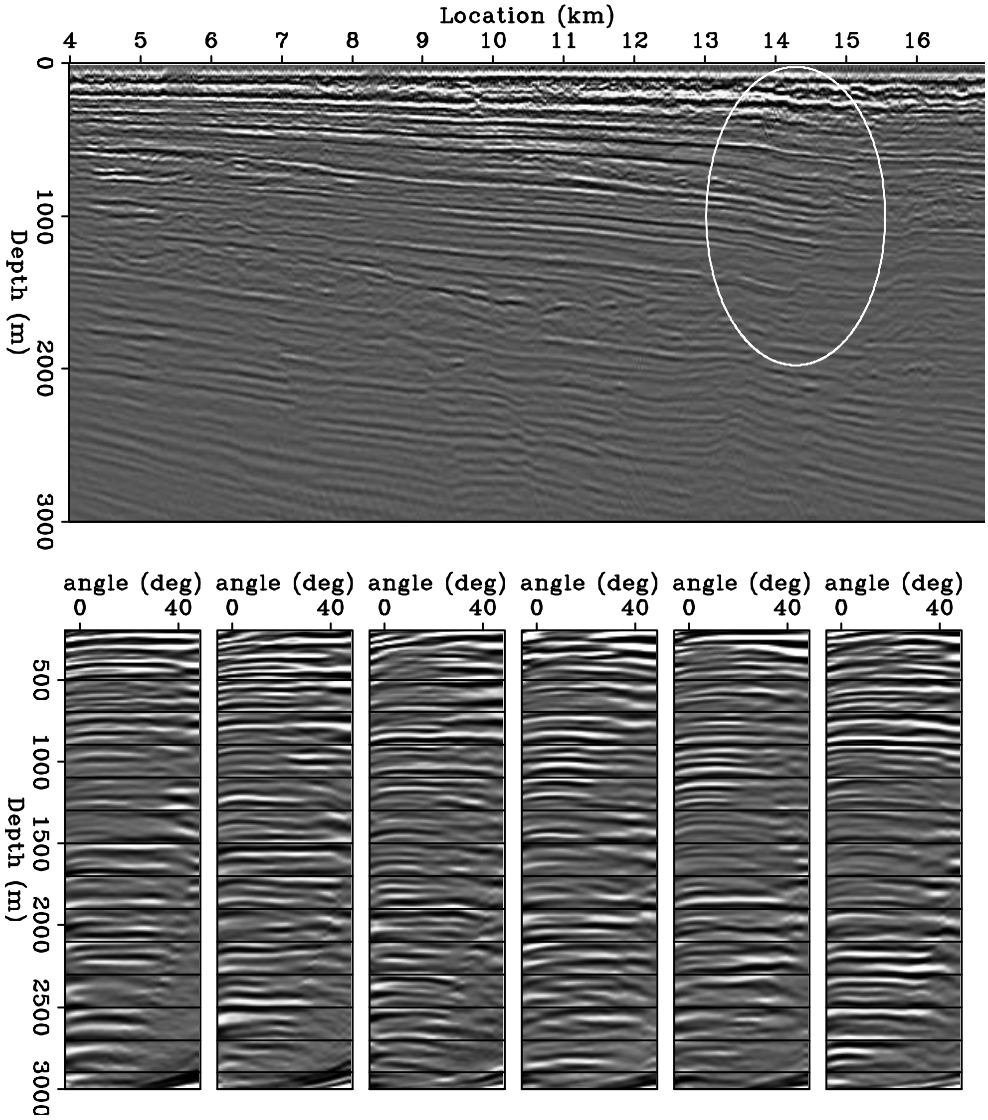

Figure 5: The final stack image (Top panel) and final angle domain common image gathers at CMP $= 7, 10, 13, 14, 14.5, 15$ km (Bottom row). Compared with Figure 4, improvements in continuity and enhancements in amplitude strength are highlighted by the oval. [**CR**]

Bakulin, A., M. Woodward, D. Nichols, K. Osypov, and O. Zdraveva, 2010a, Building tilted transversely isotropic depth models using localized anisotropic tomography with well information: Geophysics, **75**, 27–36.

———, 2010b, Localized anisotropic tomography with well information in VTI media: Geophysics, **75**, 37–45.

Bear, L., T. Dickens, J. Krebs, J. Liu, and P. Traynin, 2005, Integrated velocity model estimation for improved positioning with anisotropic PSDM: The Leading Edge, 622–634.

Biondi, B. and P. Sava, 1999, Wave-equation migration velocity analysis: SEG Expanded Abstract, **69**, 1723–1726.

Cai, J., Y. He, Z. Li, B. Wang, and M. Guo, 2009, TTI/VTI anisotropy parameters estimation by focusing analysis, part i: theory: SEG Expanded Abstracts, **28**.

Claerbout, J. F., 2009, Image estimation by example.

Clapp, R., 2000, Geologically constrained migration velocity analysis: PhD thesis, Stanford University.

Fei, T. W. and C. L. Liner, 2008, Hybrid fourier finite-difference 3D depth migration for anisotropic media: Geophysics, **73**, S27.

Fletcher, R., X. Du, and P. J. Fowler, 2009, Stabilizing acoustic reverse-time migration in TTI media: SEG Expanded Abstracts, **28**.

Helbig, K., 1956, Die ausbreitung elastischer Wellen in anisotropen Medien: Geophys. Prosp., **04**, 70–81.

Li, Y. and B. Biondi, 2011, Migration velocity analysis for anisotropic models: SEG Expanded Abstract, **30**, 201–206.

Li, Y., D. Nichols, K. Osypov, and R. Bachrach, 2011, Anisotropic tomography using rock physics contraints: 73^{rd} EAGE Conference & Exhibition.

McCollum, B. and F. Snell, 1932, Asymmetry of sound velocity in stratified formations: Physics (Journal of Applied Physics), **2**, 174–185.

Plessix, R.-E., 2006, A review of the adjoint-state method for computing the gradient of a funtional with geophysical applications: Geophysical Journal International, **167**, 495–503.

Postma, G. W., 1955, Wave propagation in a stratified medium: Geophysics, **20**, 780–806.

Sarkar, D. and I. Tsvankin, 2003, Analysis of image gathers in factorized VTI media: Geophysics, **68**, 2016–2025.

———, 2004, Migration velocity analysis in factorized VTI media: Geophysics, **69**, 708–718.

Sava, P. and B. Biondi, 2004a, Wave-equation migration velocity analysis-I: Theory: Geophysical Prospecting, **52**, 593–606.

———, 2004b, Wave-equation migration velocity analysis-II: Examples: Geophysical Prospecting, **52**, 607–623.

Sava, P. and S. Formel, 2006, Generalized imaging conditions for wave equation migration: CWP Report, **524**.

Shan, G., 2009, Optimized implicit finite-difference and fourier finite-difference migration for VTI media: Geophysics, WCA189–WCA197.

Shen, P., 2004, Wave-equation migration velocity analysis by differential semblance

optimization: PhD thesis, Rice University.
Symes, W. W. and J. Carazzone, 1991, Velocity inversion by differential semblance optimization: Geophysics, **56**, 654–663.
Takanashi, M. and I. Tsvankin, 2012, Migration velocity analysis for TI media in the presence of quadratic lateral velocity variation: Geophysics, **77**, U87–U96.
Tarantola, A., 1984, Inversion of seismic reflection data in the acoustic approximation: Geophysics, **49**, 1259–1266.
Thomsen, L., 1986, Weak elastic anisotropy: Geophysics, **51**, 1954–1966.
Woodward, M. J., D. Nichols, O. Zdraveva, P. Whitfield, and T. Johns, 2008, A decade of tomography: Geophysics, **73**, VE5VE11.
Yuan, J., X. Ma, S. Lin, and D. Lowrey, 2006, P-wave tomographic velocity updating in 3d inhomogeneous VTI media: SEG Expanded Abstracts, **25**.
Zhang, Y. and H. Zhang, 2009, A stable TTI reverse time migration and its implementation: SEG Expanded Abstracts, **28**.
Zhou, H., D. Pham, and S. Gray, 2004, Tomographic velocity analysis in strongly anisotropic TTI media: SEG Expanded Abstracts, **23**.
Zhou, H., D. Pham, S. Gray, and B. Wang, 2003, 3-d tomographic velocity analysis in transversely isotropic media: SEG Expanded Abstracts, **22**.